

# Geochemistry, Geophysics, Geosystems



#### RESEARCH ARTICLE

10.1029/2021GC010127

Paraskevi Io Ioannidi and Kyle Bogatz contributed equally to this work.

#### **Key Points:**

- Field observations of the Papoose
  Flat pluton show frictional failure of
  isolated feldspar clasts in the granitic
  pluton matrix
- 2D numerical models of two-phase systems confirm frictional failure of clasts embedded in a creeping matrix
- In the absence of clast interactions, the extent of clast failure depends on matrix viscosity and their proximity to other clasts

#### **Supporting Information:**

Supporting Information may be found in the online version of this article.

#### Correspondence to:

P. I. Ioannidi, ioannidi.iop@gmail.com

#### Citation:

Ioannidi, P. I., Bogatz, K., & Reber, J. E. (2022). The impact of matrix rheology on stress concentration in embedded brittle clasts. *Geochemistry, Geophysics, Geosystems*, 23, e2021GC010127. https://doi.org/10.1029/2021GC010127

Received 26 AUG 2021 Accepted 17 FEB 2022

#### **Author Contributions:**

Conceptualization: Paraskevi Io Ioannidi, Jacqueline E. Reber Data curation: Paraskevi Io Ioannidi, Kyle Bogatz

**Formal analysis:** Paraskevi Io Ioannidi, Kyle Bogatz

**Funding acquisition:** Jacqueline E. Reber

**Investigation:** Paraskevi Io Ioannidi, Kyle Bogatz

**Methodology:** Paraskevi Io Ioannidi, Kyle Bogatz, Jacqueline E. Reber

#### © 2022. The Authors.

This is an open access article under the terms of the Creative Commons Attribution License, which permits use, distribution and reproduction in any medium, provided the original work is properly cited.

### The Impact of Matrix Rheology on Stress Concentration in Embedded Brittle Clasts

Paraskevi Io Ioannidi<sup>1</sup>, Kyle Bogatz<sup>1</sup>, and Jacqueline E. Reber<sup>1</sup>

<sup>1</sup>Department of Geological and Atmospheric Sciences, Iowa State University, Ames, IA, USA

**Abstract** Frictional failure is the dominant deformation mechanism for rocks in the upper crust while in the middle crust rocks begin to deform viscously. Within this transition, brittle and viscous phases coexist, forming semi-frictional materials. While semi-frictional deformation on large scales might play an important role in understanding the transition between earthquakes and slow slip/creep, it can also be observed at smaller scales. Here, we use field observations of the Papoose Flat pluton in eastern California to study deformation of heterogeneous materials during shearing. Clast concentration varies between 2% and 12% by area. Field and microscopic observations show that the matrix deforms viscously, while the clasts fail in a brittle manner. We systematically document clast concentration and spacing with respect to clast fracturing and observe increasing frictional failure of clasts with increasing clast concentration. To test which matrix viscosities impose enough stresses on the clasts to lead to frictional deformation, we complement field observations with 2D numerical models. Maps with 7% by area randomly placed circular clasts are created and deformed under simple shear kinematic conditions. We test different matrix viscosities, from constant low and high viscosity (10<sup>17</sup> and 10<sup>19</sup> Pa.s, respectively), to dislocation creep for granite. Clasts in the vicinity of other clasts are affected by stresses around their neighbors. This effect decreases with increasing clast distance. Our field observations and numerical results suggest that the viscous phase can impose significant stresses onto the brittle phase, causing failure even at very low clast concentrations and in the absence of clast-clast interactions.

#### 1. Introduction

Frictional failure is the dominant deformation mechanism for rocks within the upper crust while in the middle crust rocks begin to deform by viscous processes. It has been well established that within this transition frictional and viscous phases coexist, forming semi-frictional materials (e.g., Behr & Bürgmann, 2021; Bürgmann, 2018; Scholz, 1998). These materials are expected to have complex rheological properties that diverge from purely brittle/frictional and purely viscous end-members. Throughout this manuscript, we will be using the terms brittle and frictional interchangeably. By combining the time scales of fast, brittle deformation with the time scales of slow, continuous creep, semi-frictional materials have the potential to lead to various strain transients when deforming (Beall et al., 2019a; Birren & Reber, 2019; Fagereng & Sibson, 2010; Lavier et al., 2013; Reber et al., 2014; Webber et al., 2018). While semi-frictional deformation on a large scale might play an important role in the understanding of the transition between fast earthquakes and slow slip and creep (e.g., Behr & Bürgmann, 2021; Behr et al., 2018; Kirkpatrick et al., 2021), it is a phenomenon that can also be observed at relatively small spatial scales (e.g., Handy, 1990). Furthermore, semi-frictional deformation can be observed in a wide variety of lithologies (e.g., Fusseis et al., 2006; Gapais et al., 1987; Hayman & Lavier, 2014; Jammes et al., 2015; Mitra, 1976; Wakefield, 1977).

Clasts embedded in a viscous matrix have been the focus of a wide range of studies using a variety of approaches such as field investigations, analog experiments, numerical modeling and analytical studies. Studies can be divided into two broad groups depending on the strength of the clasts with respect to the matrix; (a) clasts that are stronger than the matrix, and (b) clasts that are weaker than the matrix where in an extreme case the clasts can be voids in the matrix. The aims of these studies are as varied as the investigation approaches, and we would like to refer the reader to Marques et al. (2014) for a more complete overview of the literature on embedded clasts.

Experiments and theoretical considerations using low brittle phase concentrations that are not actively deforming have shown that the addition of a strong brittle phase to a weaker, purely viscous system, leads to an increase in effective viscosity (Einstein, 1905; Roscoe, 1952). Studies concentrating on semi-frictional deformation in rocks have identified that besides the volume fraction of the two phases, the competency or strength contrast

IOANNIDI ET AL. 1 of 19



**Project Administration:** Jacqueline E. Reber

**Resources:** Paraskevi Io Ioannidi, Jacqueline E. Reber

Software: Paraskevi Io Ioannidi, Kyle

Bogatz

Supervision: Jacqueline E. Reber Validation: Paraskevi Io Ioannidi, Kyle Bogatz, Jacqueline E. Reber Visualization: Paraskevi Io Ioannidi, Kyle Bogatz, Jacqueline E. Reber Writing – original draft: Paraskevi Io Ioannidi, Kyle Bogatz, Jacqueline E. between the brittle and viscous phases is a primary controller on the deformation mechanics and dynamics of semi-frictional systems (Handy, 1990; Holyoke & Tullis, 2006; Johnson et al., 2004; Jordan, 1987). Depending on the volume fraction and the competency contrast, deformation localizes either in the brittle, the viscous, or both phases. For low brittle phase concentrations, the system is primarily matrix supported and deformation is controlled by the rheological properties of the viscous phase. Two deformation domains can be distinguished at low brittle phase concentrations, based on competency contrasts between the viscous and brittle phases. Previous studies have shown that when there is a high competency contrast and the brittle phase concentration is lower than 30%, the brittle phase remains passive and the viscous phase will dominate bulk rheology (Holyoke & Tullis, 2006; Jordan, 1987). At low competency contrasts the brittle phase is capable of deforming, actively contributing to the bulk rheology. When the brittle phase concentration is high, and a clast supported system is present, bulk rheology is mainly controlled by the brittle phase. Stress applied to such systems manifests itself in the formation of force chains, frictional sliding, and fracturing (Handy, 1990; Holyoke & Tullis, 2006; Johnson et al., 2004; Jordan, 1987; Li et al., 2007). However, even in systems with a high brittle phase concentration, the rheological properties of the viscous phase can still impact strain localization and deformation dynamics (Higashi & Sumita, 2009; Ladd & Reber, 2020; Reber et al., 2014). Experimental studies have revealed that the addition of a relatively small amount of viscous phase leads to increased localization and can dampen the frictional stick-slip deformation signature (Higashi & Sumita, 2009; Reber et al., 2014).

Slow-slip events have been linked to the presence of strong and weak phases, where altering clast- or matrix-supported rheology leads to either fast-slip (earthquakes) or slow-slip events (Beall et al., 2019b; Fagereng & Sibson, 2010; Lavier et al., 2013; Webber et al., 2018). Numerical studies have proposed that a critical concentration of the brittle phase is necessary to create conditions suitable for seismic activity (Beall et al., 2019a; Webber et al., 2018). In the presence of <50% by volume strong clasts, the deformation is controlled by continuous creep (Beall et al., 2019a; Ioannidi et al., 2021). For clast concentrations higher than 50% by volume, clasts can interact with each other and force chains or stress bridges can form (Beall et al., 2019a; Webber et al., 2018). In cases where the clast concentration is smaller, direct coupling between the viscous matrix material and the clasts, and matrix properties that can temporarily sustain differential stresses (Ladd & Reber, 2020) would be necessary to transfer stresses leading to the potential failure of clasts (Phillips et al., 2020).

Here, we present macroscopic field observations from the Papoose Flat pluton, a semi-frictional system that displays varying brittle clast concentrations. We identify a relationship between brittle clast concentration and the degree of brittle failure while focusing on solid state post emplacement deformation. Numerical experiments complement field observations by systematically investigating the effect of clast spacing and matrix rheology on stress concentrations in the brittle clasts at low shear strains. Field observations and numerical results suggest that the viscous phase can impose significant differential stress onto the brittle phase, causing failure even at very low clast concentrations and in the absence of clast-clast interactions.

#### 2. Papoose Flat Pluton: Geological Setting and Field Observations

#### 2.1. Geological Background

The Papoose Flat pluton is a granodioritic igneous intrusion within the White-Inyo Range of eastern California. Emplacement occurred in the Cretaceous at temperatures and depths of 400°C–500°C and 12–15 km, respectively (de Saint-Blanquat et al., 2001). At present, the Papoose Flat pluton is an East-West trending ellipsoid covering 83 km² (Figure 1). It consists of a typical granitic-granodioritic composition with a quartz and micarich matrix and embedded feldspar clasts. The average composition of the pluton is 42% plagioclase, 33% quartz, 19% K-feldspar, and 6% other minerals, including primary muscovite and biotite (Ross, 1966). Feldspar clasts, predominantly plagioclase, are significantly larger in size than the grains observed in the matrix (de Saint-Blanquat et al., 2001). Feldspar clasts seem to have rotated minimally. While in the middle of the pluton, the feldspar clasts do not form a shape preferred orientation, closer to the pluton rim they show a slight shape preferred orientation parallel to the magmatic foliation (de Saint-Blanquat et al., 2001). The feldspar clasts range in diameter from 0.5 mm to 2.5 cm, while the quartz grains in the matrix range from 0.05 to 1.5 mm in diameter. Inclusions of micas and quartz are abundant within feldspar clasts. Microstructures vary from unmodified magmatic structures in the center of the pluton to medium-temperature plastic (quartz) and brittle (feldspar) deformation at the rim (de Saint-Blanquat et al., 2001). With a decrease in temperature from the pluton center to the rim, fractures

IOANNIDI ET AL. 2 of 19



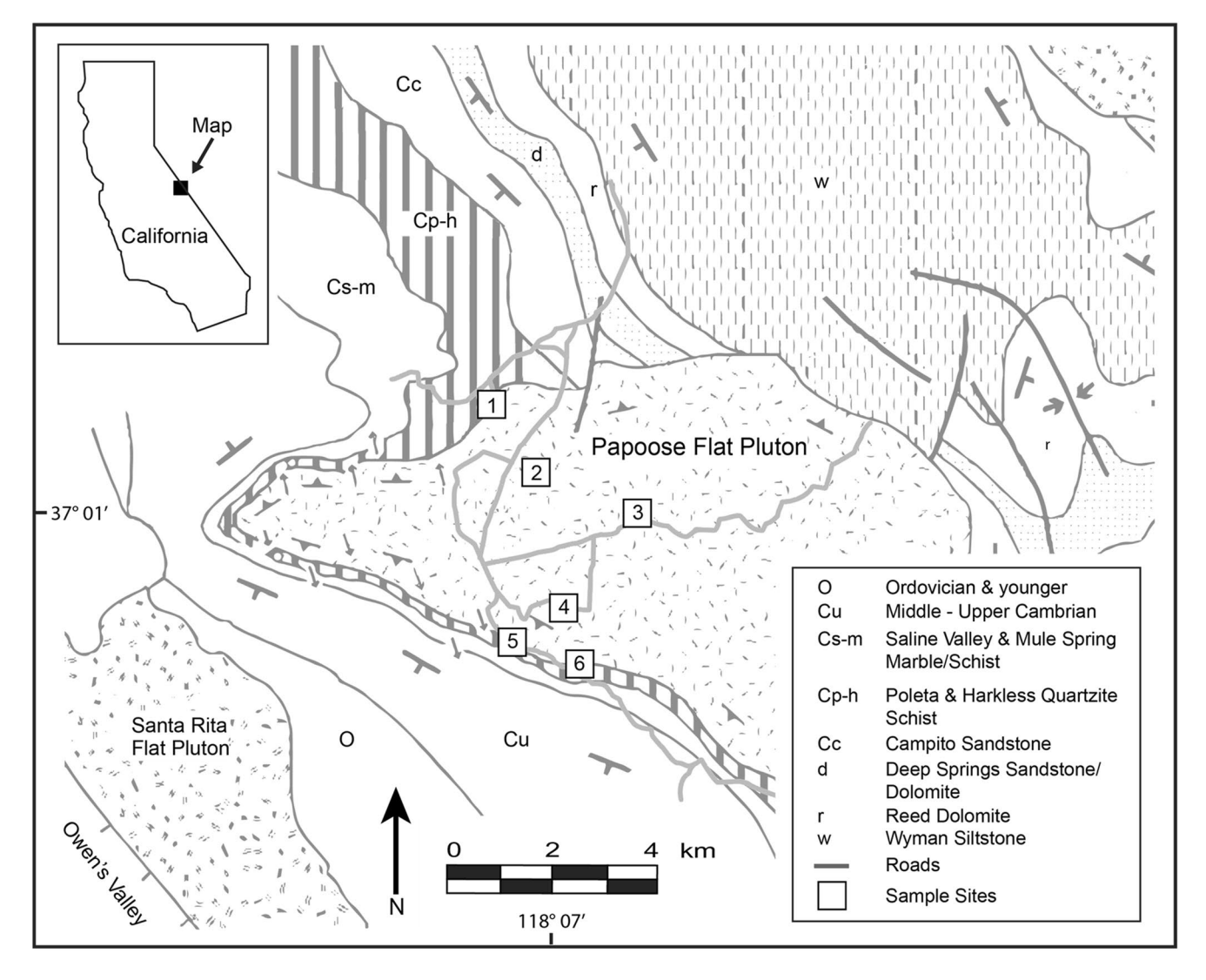


**Figure 1.** Simplified geologic map of Papoose Flat pluton area. Numbers refer to sample locations as described in the text. GPS sample locations can be found in Table S1 in Supporting Information S1. Adapted from Morgan et al. (2000).

within the feldspar clasts become more common (de Saint-Blanquat et al., 2001; Morgan et al., 2000). Mode I and mode II fractures can be observed at the hand sample scale, where mode II fractures display modest shear offset (Figure 2). In addition, on the micro-scale, the feldspar clasts display an abundance of mode I fractures. The matrix away from the center of the pluton displays signs of viscous flow through the formation of quartz ribbons, elongated clusters of quartz grains and alignment of platy minerals such as muscovite and biotite (Figure 2; de Saint-Blanquat et al., 2001). Quartz grains show lobate boundaries and little to no undulose extinction, suggesting that grain boundary migration and grain boundary area reduction are the primary micro-deformation mechanisms. This implies that quartz deformed in a viscous manner, although there is some evidence of static recrystallization (de Saint-Blanquat et al., 2001; Hirth & Tullis, 1992; Passchier & Trouw, 2005).

The coexistence of a viscous quartz- and mica-rich matrix and brittle feldspars is seen throughout the pluton; however, previous observations indicate that the concentration of feldspar clasts decreases toward the center of the pluton, farther from the pluton and host rock contact (de Saint-Blanquat et al., 2001). We observe a decrease of large feldspar clasts from 12% by area at the rim of the pluton to 2% by area in its center, confirming earlier observations.

IOANNIDI ET AL. 3 of 19

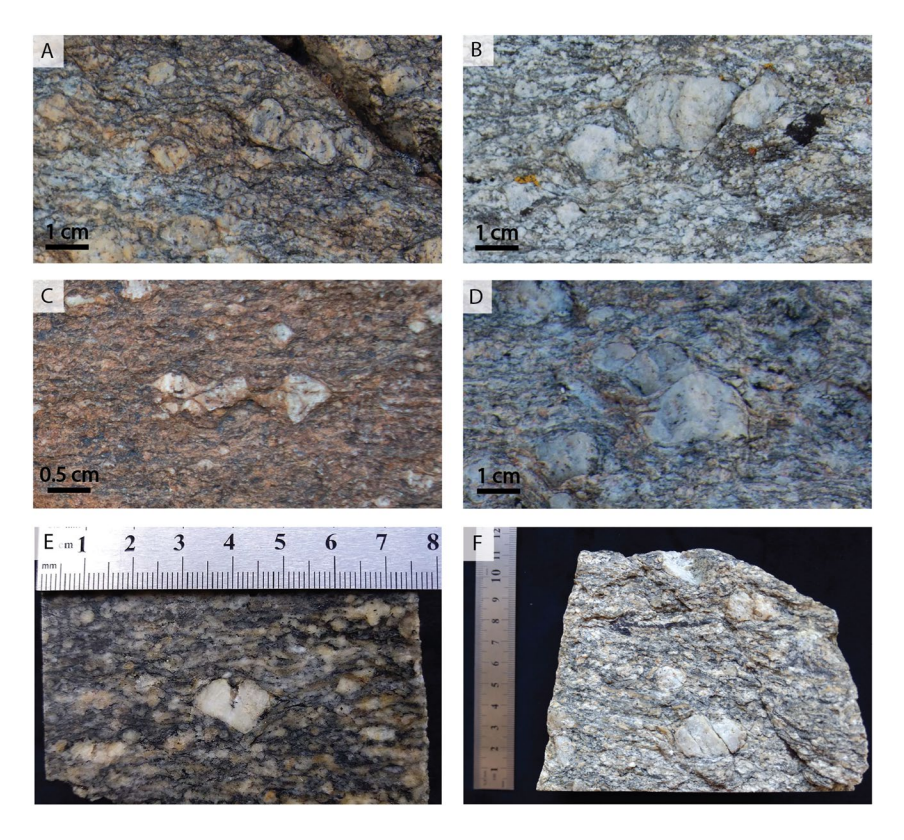


**Figure 2.** Example collection of fractured feldspar clasts. Panels (a–d) show outcrop photographs, panel (e) shows cut hand sample, and panel (f) shows uncut hand sample.

The deformation history and associated deformation of the Papoose Flat pluton itself remains somewhat opaque. Intrusion models from a single stage (Sylvester et al., 1978) to multiple stages (Morgan et al., 1998) have been suggested. The most recent field observations and numerical models suggest that the pluton formed through the emplacement of several magma pulses (Chen & Nabelek, 2017; de Saint-Blanquat et al., 2001). Based on their numerical models, Chen and Nabelek (2017) advocate for an incremental growth model for the pluton formation with an intrusion strain rate of  $2.5 \times 10^{-8} \, \mathrm{s}^{-1}$ , while a background strain rate of  $10^{-15} \, \mathrm{s}^{-1}$  is considered for the crustal domain.

Paterson et al. (1991) reported no magmatic foliation and only one example of weakly aligned feldspar clasts in the center of the pluton. de Saint-Blanquat et al. (2001) documented an increase in foliation density from the pluton center to the margin. In areas away from the pluton center, they document S-C fabrics and some ductile shear zones, indicating that the pluton rim underwent some shear deformation. They, however, record conflicting observations where only on the outcrop scale shear deformation is observable, but not on the micro scale. The medium-temperature plastic and brittle deformation observable closer to the rim of the pluton is suggested to have occurred while magma was still flowing in the middle of the pluton (de Saint-Blanquat et al., 2001). This solid-state deformation has only rarely lead to alignment of feldspar clasts (Paterson et al., 1991). While we include data from the center of the pluton in our field data (area 3 in Figure 1) we focus the numerical analysis (see Section 3) on deformation conditions closer to the rim of the pluton.

#### 2.2. Distribution of Fractured Clasts in the Pluton

#### 2.2.1. Data Collection

To quantify the spatial distribution of frictional deformation, traces of outcrops are made to determine the abundance and physical characteristics of the fractured clasts (Figures 4a and 4b). A total of 64 outcrops of  $30 \times 30$  cm are mapped within six regions of the pluton in order to incorporate spatial variability (Figure 1). Pieces of

IOANNIDI ET AL. 4 of 19



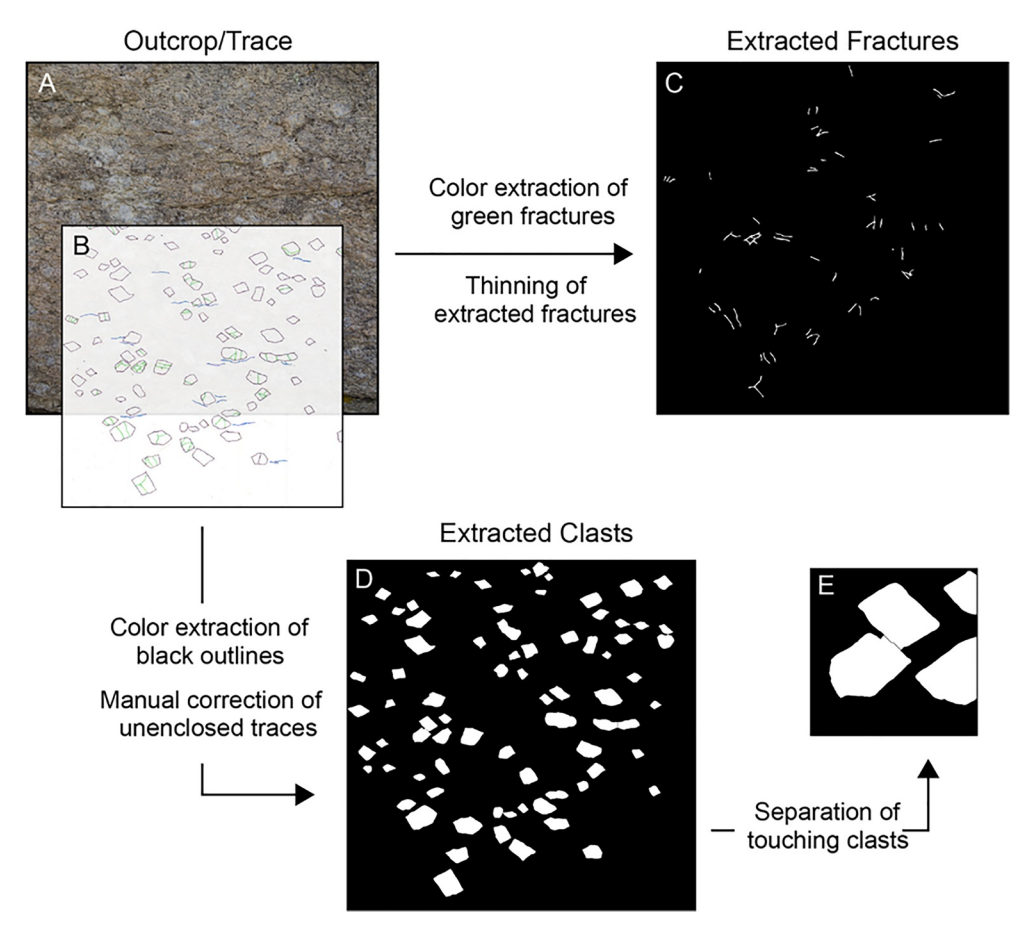


**Figure 3.** Schematic illustrating the systematic extraction of clast properties. (a) Photograph of outcrop, (b) traces produced from outcrop, (c) fractures extracted from trace via color extraction, (d) clast extraction from trace, and (e) zoom in on two touching clasts that are separated via a watershed function.

transparent plastic are taped to representative sections of lineation parallel outcrops, avoiding heterogeneities such as veins or post emplacement weathering. All clasts larger than 0.5 cm are outlined in black marker. Fractures within the clasts are traced in green and the flow pattern within the mica-rich matrix is marked in blue. Flow patterns are recorded to ensure each trace is collected at a similar orientation. Note that we are not distinguishing between mode I and II when tracing the fractures. We also only trace fractures that are well visible through the transparent plastic without any magnification. Inside each of the six sampling regions, the number of traces taken is dictated by outcrop availability and ranges from six to 18. GPS coordinates are recorded at each site to determine the sample distance from the pluton contact and consecutive samples are taken in a transect toward the center of the pluton to further capture the effect of the pluton contact's proximity (data table in Table S1 in Supporting Information S1, trace files are provided in Data set S1 in Supporting Information S1). All traces are then scanned to produce electronic copies that are input into a MATLAB code summarized in Figure 3. Clasts, fractures, and matrix flow lines are isolated using color extraction. Due to the inconsistency of ink on plastic, threshold values for each color are needed. In some cases, this results in incomplete traces around clasts which are manually corrected by enclosing them with an approximated boundary. Once all clasts are identified, touching clasts are separated. Each clast/group of clasts is evaluated by using a watershed function. In a first step, any pinching/narrowing of the outline of the clast group is identified. If narrowing is detected, the clast group is separated along a straight line along the shortest distance between the two sides of the clast group. This way, the clast group gets divided into individual clasts (Figure 3e). At this point, the clast population and clast area are calculated for each trace.

IOANNIDI ET AL. 5 of 19

Standard deviation

Minimum

Maximum

Average

Standard deviation

29.1

2%

12%

7%

2%



Summary of Variables Calculated From 64 Traces									
		Number of clasts	Total clast area (cm <sup>2</sup> )	Cumulative fracture length (cm)	Clast concentration				
Unfractured clasts	Minimum	4	7.5	-	-				
	Maximum	88	132.6	-	-				
	Average	28	53.6	-	-				
	Standard deviation	15	29.8	-	-				
Fractured clasts	Minimum	2	6.9	2.1	-				
	Maximum	66	140.6	136.2	-				
	Average	19	53.6	33.6	_				

32.5

36.1

194.1

107.3

33.0

15

12

123

47

23

Color extraction is also used to isolate the fractures from the clasts (Figure 3c). The extracted fractures are thinned to the width of a single pixel, allowing for them to be characterized by their length (the sum of their pixels). Each fracture is assigned to its respective clast based on location. This allows for each clast to be identified based on the condition of being fractured or not fractured.

#### **2.2.2.** Results

Table 1

Total

To investigate the relationship between clast concentration and failure of the clasts, the following metrics are calculated from each trace: clast concentration, number of clasts, area of clasts, total fracture length, and fracture status of clasts. The range, averages, and standard deviations for these quantities are summarized in Table 1. In addition, we record the aspect ratio and area of each clast (Figure 4). We document a total of 3,113 clasts of which 1,255 are fractured. The mean clast area is 1.27 cm<sup>2</sup> with a standard deviation of 1.17. The mean aspect ratio is 1.66 with a standard deviation of 0.65. Note that Figure 4 shows the total clast data including fractured and unfractured clasts. The area taken up by the fractures in fractured clasts is ignored in the area measurements.

We observe a clast concentration ranging between 2% by area to 12% by area. The higher concentration is found close to the edge of the pluton, the lowest concentration is found in the middle of the pluton. To quantify the degree of brittle failure we report the number of fractured clasts, the area of fractured clasts, and the total fracture lengths in each trace. Each of these is compared to the total clast concentration within the trace to determine if there is a relationship between clast concentration and the degree of failure within the clasts. A positive correlation is seen between clast concentration and number of fractured clasts (Figure 5a). Higher clast concentrations correspond to more fractured clasts. The relationship between these two characteristics is not particularly strong, with an  $R^2$  value of 0.27. Using the total area of fractured clasts as representative for the degree of fracturing produces a slightly stronger positive correlation with an  $R^2$  value of 0.34 (Figure 5b). Lastly, when plotting the total fracture length against clast concentration, we observe that the total fracture length also increases with increasing clast concentration. This correlation is the weakest, with an  $R^2$  value of 0.12 (Figure 5c).

Although clast concentration is only loosely correlated to the number of fractured clasts, area of fractured clasts, and total fracture length, together they all indicate that an increase in clast concentration leads to an increase in the degree of brittle failure. In all our analyzed sections, the concentration of clasts was not high enough for clasts to be in systematic contact with each other. In some cases, clasts are touching but they do not form extended "chains" of clasts that would be able to form an interconnected load bearing framework. In almost all sections, we observe clasts that are displaying fractures which are not in contact with any neighboring clast. However, the distance to a neighboring clast is in most cases smaller than two times the diameter of the fractured clast. This suggests that the clast concentration has an influence on strain distribution within the semi-frictional system in the absence of direct clast-to-clast interactions.

IOANNIDI ET AL. 6 of 19



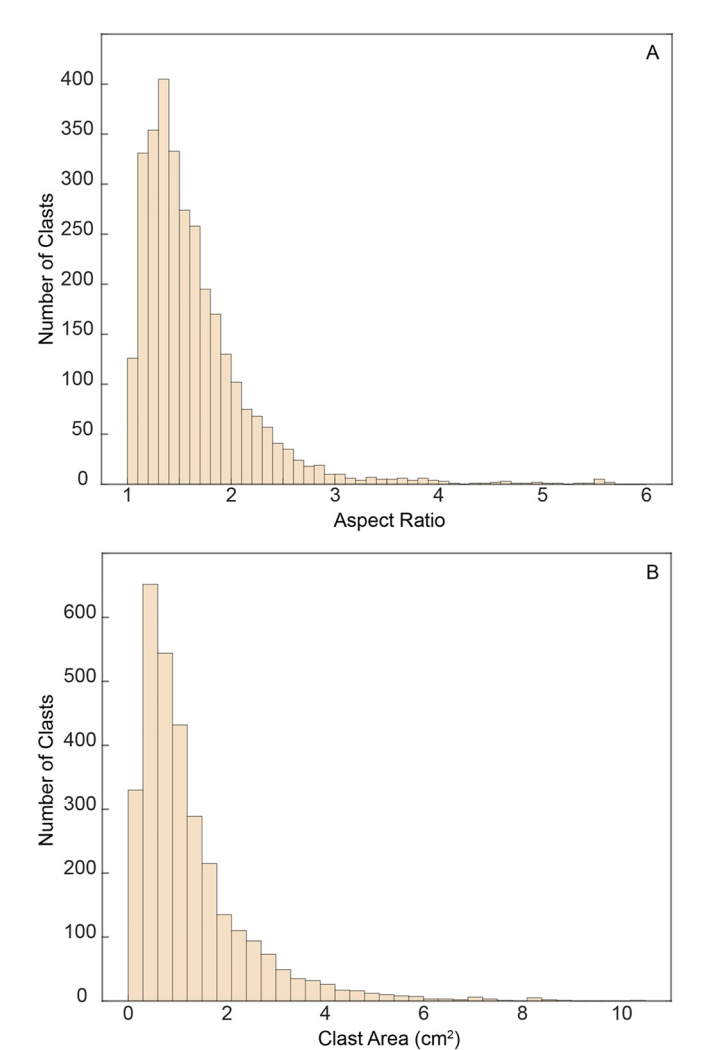


**Figure 4.** Aspect ratio (a) and clast area (b) distribution of all recorded clasts. *Note.* Fractured and unfractured clasts are combined and that fracture area and shear offset are ignored.

 $120 \times 39$  m (Figure 6).

#### 3. Numerical Models of Stress Distribution

We conduct a series of numerical experiments aimed at examining: (a) the impact of clast spacing on the deformation of clasts and matrix, and (b) the effect of matrix viscosity on strain distribution and stress concentration in the clasts. For the first objective, we perform numerical simulations on simple configurations of two clasts placed at different distances within a viscous matrix. To tackle the second question, we model the deformation of a "digital outcrop" comprising 7% of clasts by area, with various matrix viscosities. We show what parameters cause stress concentrations in the clasts that would lead to clast fracturing in the natural system. Both sets of models are experiments under simple shear kinematic conditions using the 2D version of the open-source Finite Element code pTatin (May et al., 2014, 2015). The material-point-method utilized by the code allows us to track material composition, viscous, and plastic strain, and the type of yielding in each domain of our models. Viscosity evaluated on these material points is then averaged (in our models using a geometric averaging scheme), before it is projected onto the finite elements of the mesh. Details of the 2D version of the code are given in Appendix A, as well as in Jourdon et al. (2018) and Ioannidi et al. (2021). We consider the structures observed in the field to be scale independent, as suggested by recent studies (Fagereng, 2011; Grigull et al., 2012; Ioannidi et al., 2021; Le Pourhiet et al., 2013), therefore we upscale field outcrop scales to map scales (from a cm-scale to a m-scale). For more details, see Discussion on scaling (Section 5.1.1).

#### 3.1. Model Setup and Boundary Conditions

Following the  $30 \times 30$  cm trace maps introduced in the previous section, we create an initial 2D model box of  $30 \times 30$  m with a mesh resolution of  $0.15 \times 0.15$  m. Within this box, we either place 2 circular clasts in the middle with different spacing (objective 1), or we randomly place circular inclusions (Figure 6) until their area percentage reaches 7% (objective 2), which is the average clast concentration observed in the field area. Our randomly generated 7% map is similar to what is found in the Papoose Flat pluton with areas where clasts either form clusters or are isolated.

The diameter of the clasts in both cases is 1.5 m, and each clast contains  $\sim$ 80

finite elements. To avoid boundary effects, in all maps we add 45 m of matrix to the left and the right (Figure 6), resulting in a total length of 120 m for each model. We also add extra matrix at the top and bottom equal to 6 times the clast size, that is, 9 m; this way, we avoid potential boundary effects from incompressible clasts being close to the model boundary where velocity is applied. The final 2D map is

We choose kinematic simple shear conditions, shown in Figure 6. Horizontal x-parallel velocities ( $v_s$ ) are applied at the top and bottom of the domain with a magnitude of  $\pm 2 \times 10^{-10}$  m/s which, based on the width of the model, results in a background strain rate of  $\sim 10^{-11}$  s<sup>-1</sup>. This value falls within the estimated strain rates given by Chen and Nabelek (2017). Vertical velocities at the top and bottom are equal to zero and confining (lithostatic) pressure

We deform the models to modest shear strains with a maximum bulk value  $\sim$ 0.5 (or  $\sim$ 1 engineering strain). Despite the low bulk strain of the models, locally the viscous shear strain may reach up to  $\sim$ 2, and the plastic strain up to  $\sim$ 1. Based on the emplacement conditions of the pluton (400°C–500°C and 12–15 km, de Saint-Blanquat et al., 2001), we use a confining pressure of 400 MPa and a temperature of 400°C, which combined with a thermal gradient of 30° C/km, corresponds to a depth of  $\sim$ 13 km. We neglect gravity, due to the small size of the models. The models are run for 3,000 years, with an adaptive timestep of  $\sim$ 10 years. Using the total time, the initial shearing velocity and the height of the model, the expected bulk viscous strain is  $\sim$ 0.5.

IOANNIDI ET AL. 7 of 19

 $(P_{conf})$  is applied at the vertical boundaries of the model.



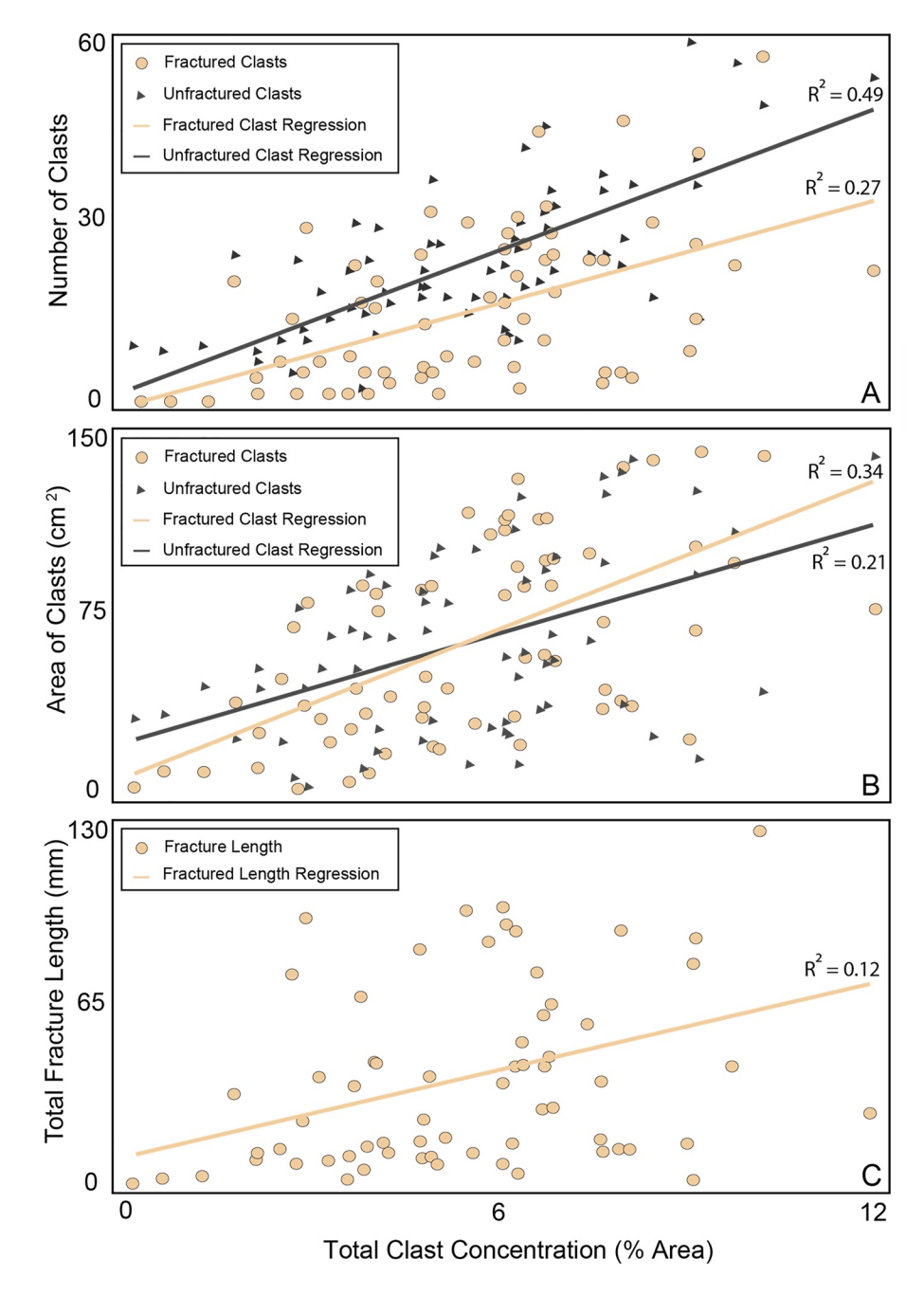
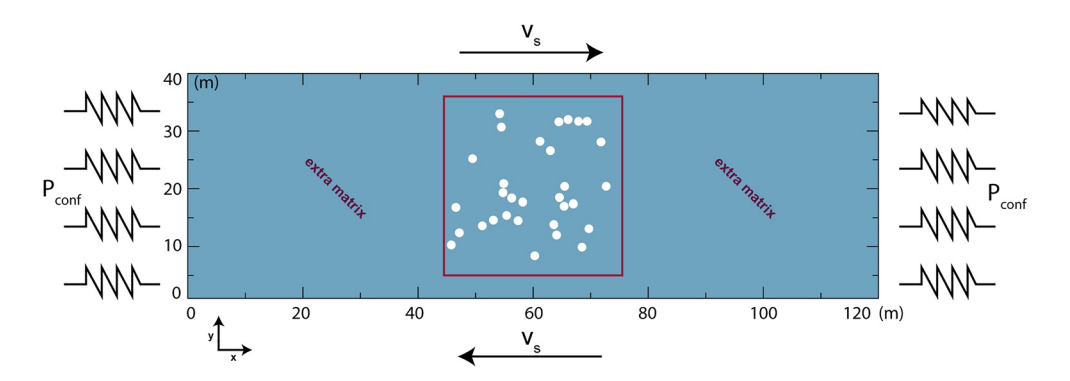


Figure 5. (a) Number of clasts versus clast concentration, (b) area of clasts vs. clast concentration, and (c) total fracture length versus clast concentration. Each data point represents the findings of one  $30 \times 30$  cm<sup>2</sup> investigation area.

#### 3.2. Material Parameters

Our 2D maps comprise visco-plastic clasts and matrix. The frictional strength of both phases is limited by Byerlee's law (20 MPa and 30° for cohesion and angle of friction, respectively). At the pressure and temperature conditions of the pluton, the clasts show no viscous deformation; therefore, we use a constant viscosity of  $10^{22}$  Pa.s to model the clasts. This has the added benefit of saving on computation time. This viscosity value is too high to be active during deformation, which enables us to model only the brittle nature of the observed feldspar clasts. For the matrix in our two-clast models, we use a constant viscosity of  $10^{17}$  Pa.s. For the matrix in our 7% models, we test different viscosity formulations: models Con17 and Con19 (Table 2) have a matrix with a constant viscosity of  $10^{17}$  and  $10^{19}$  Pa.s, respectively; model DC employs a dislocation creep formulation for

IOANNIDI ET AL. 8 of 19



**Figure 6.** Model setup and boundary conditions used. Red box shows the initial model of 7% by area clasts, before the addition of extra matrix. For detailed explanation, see text.

the matrix viscosity. Since the plutonic matrix in the field consists of granite, we chose the creep parameters for Westerly granite (Carter et al., 1981; Kirby & Kronenberg, 1987) to model it numerically. To further investigate the effect of matrix rheology on the deformation of the clasts, we use 10 times weaker and 10 times stronger dislocation creep law (DC\_weak and DC\_strong, respectively). To produce these modified flow laws, we multiply the A parameter in the dislocation creep law ( $\dot{\varepsilon} = A\sigma^n \exp\left(\frac{-Q}{RT}\right)$ ) by 10 and 0.1, respectively. Details of the different matrix rheologies are given in Table 2, while the dislocation creep parameters are explained in Appendix A1 and a graphical representation of the viscous strength of the models is given in Figure A1. More details on the choice of the particular flow law are given in Text S1, Figure S1 and Table S1 in Supporting Information S1.

The maximum plastic cut-off is limited by 500 MPa von Mises stresses; similarly, the minimum cut-off for plasticity is 10 MPa for tensile failure. This means that tensile fractures cannot form in our models, but we are able to assess the areas where they would occur. Given the general appearance of distributed plastic deformation in our study area, we do not use plastic softening, which tends to localize deformation along distinct shear zones.

To understand the effect of clast spacing on stress localization within the matrix and in the clasts, we create maps with two clasts at varying distances and orientations to each other: the distance between two clasts is equal to 1.5, 4.5, or 7.5 m (which is equal to 1, 3, and 5 times their diameter; Figure 7). For each of these distances, we create models where the line connecting the centers of the clasts forms a  $0^{\circ}$  or  $45^{\circ}$  angle to the shear plane (Figure 7). For these models, we keep the matrix viscosity constant at  $10^{17}$  Pa.s.

## Table 2 Rheological Properties for the Matrix of Different Models

Model	Viscosity type	Viscosity value	A (MPa <sup>-n</sup> s <sup>-1</sup> )	n	Q (kJ/ mol)
Con17	Constant	10 <sup>17</sup> Pa.s	-	_	_
Con19	Constant	10 <sup>19</sup> Pa.s	-	_	_
DC	Power-law	-	$1.25 \times 10^{-9}$	2.9	106
DC_weak	Power-law	-	$1.25 \times 10^{-10}$	2.9	106
DC_strong	Power-law	-	$1.25 \times 10^{-8}$	2.9	106

*Note.* Values A, n, and Q for DC models is from Carter et al. (1981) and Kirby and Kronenberg (1987).

#### 4. Numerical Results

#### 4.1. Impact of Clast Distance on Shear Stress and Strain Distribution

In the two-clast models with a constant matrix viscosity of  $10^{17}$  Pa.s, we find that the distance between the clasts affects the viscous deformation in the matrix. When the distance between the clasts is equal to their diameter (either at  $0^{\circ}$  or at  $45^{\circ}$  angle to the shearing direction, first row of Figure 7), viscous strain of the matrix is more pronounced, while at larger distances (five times their diameter; last row of Figure 7), the matrix in between is almost unaffected by their interaction. In all cases, four compressional and four dilational quadrants form around each clast: viscous strain is high in the former and low in the latter (also referred to here as "strain/stress peaks" and "strain/stress shadows"). Not surprisingly, for smaller distances between the clasts, both the "peaks" and the "shadows" are more pronounced. The distribution of shear stress follows a similar pattern: higher values can be observed in the matrix between the clasts spaced at smaller distances between the clasts. The effect of the distance between the clasts is less pronounced for clasts aligned

IOANNIDI ET AL. 9 of 19



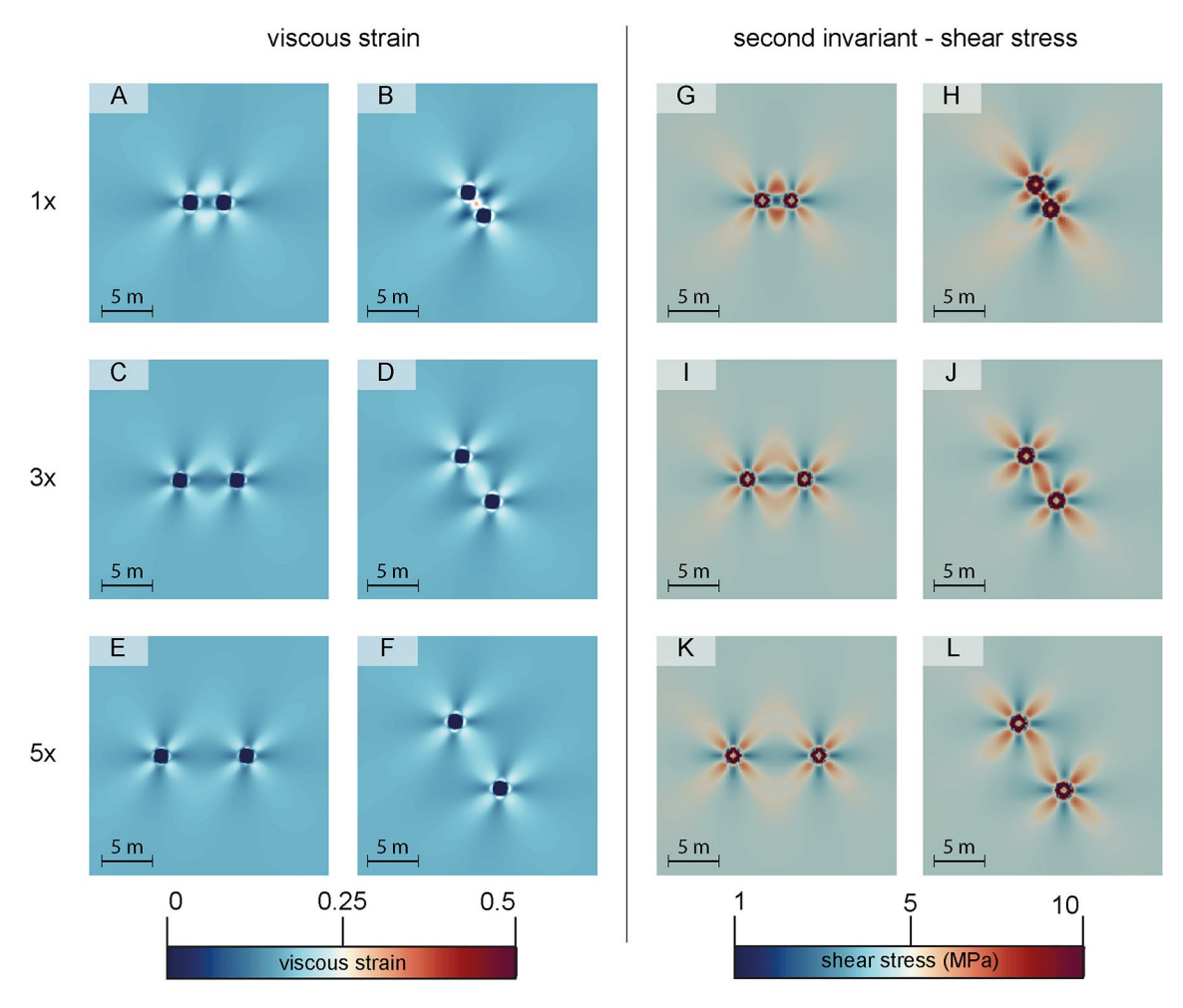


**Figure 7.** Viscous strain (a–f) and second invariant of shear stress (g–l) for two-clast models. First and third columns correspond to clasts placed parallel to the shearing direction, second and fourth column represent models where the clasts are placed at a  $45^{\circ}$  angle to the shearing direction. All models have a constant matrix viscosity of  $10^{17}$  Pa.s. The distance between the clasts is increasing from top to bottom as indicated at the left of each row (1×, 3×, and 5×). Each clast is 1.5 m in diameter.

parallel to the shear direction (compare e.g., Figures 7a and 7b etc.). This is expected, since when clasts are aligned at a  $45^{\circ}$  angle to the shear direction, their alignment is parallel to  $\sigma_1$ .

#### 4.2. Constant Matrix Viscosity

We use the model with 7% clasts to investigate the effect of matrix rheology on the distribution of stress and strain. Two main types of matrix viscosities are investigated, constant and power-law. All values mentioned from now on concern observations after 3,000 years of deformation and  $\sim$ 0.5 bulk strain.

In the Con17 model, the viscosity of the matrix and clasts shows no fluctuation, with a value of  $10^{17}$  Pa.s for the matrix, and  $10^{22}$  Pa.s for the clasts. The matrix viscosity is low enough to accommodate most of the deformation, thus leading to viscous strain localization (Figure 8a). The bulk strain is ~0.5, similar to the one calculated by the initial boundary conditions (see Section 3.1). However, locally it may go as low as ~0.2 at stress "shadows" (areas with low shear stresses), and as high as 0.7 at stress "peaks," while it can reach 1.6 in areas where the matrix is "sandwiched" between two clasts. The rims of the clasts show very little plastic strain ranging from 0.01 to 0.4 (Figure 8b). Stresses in the matrix are ~1 MPa, while this can vary between <1 MPa (stress shadows) and ~2 MPa (stress peaks, Figure 8c). Shear stresses in the clasts also fluctuate, depending on their location and proximity to other clasts. In the center of isolated clasts, shear stresses are ~1 MPa. For interacting clasts, depending on whether they are in the stress shadows of other clasts or not this value can reach up to 3 MPa. The rims of most

IOANNIDI ET AL. 10 of 19



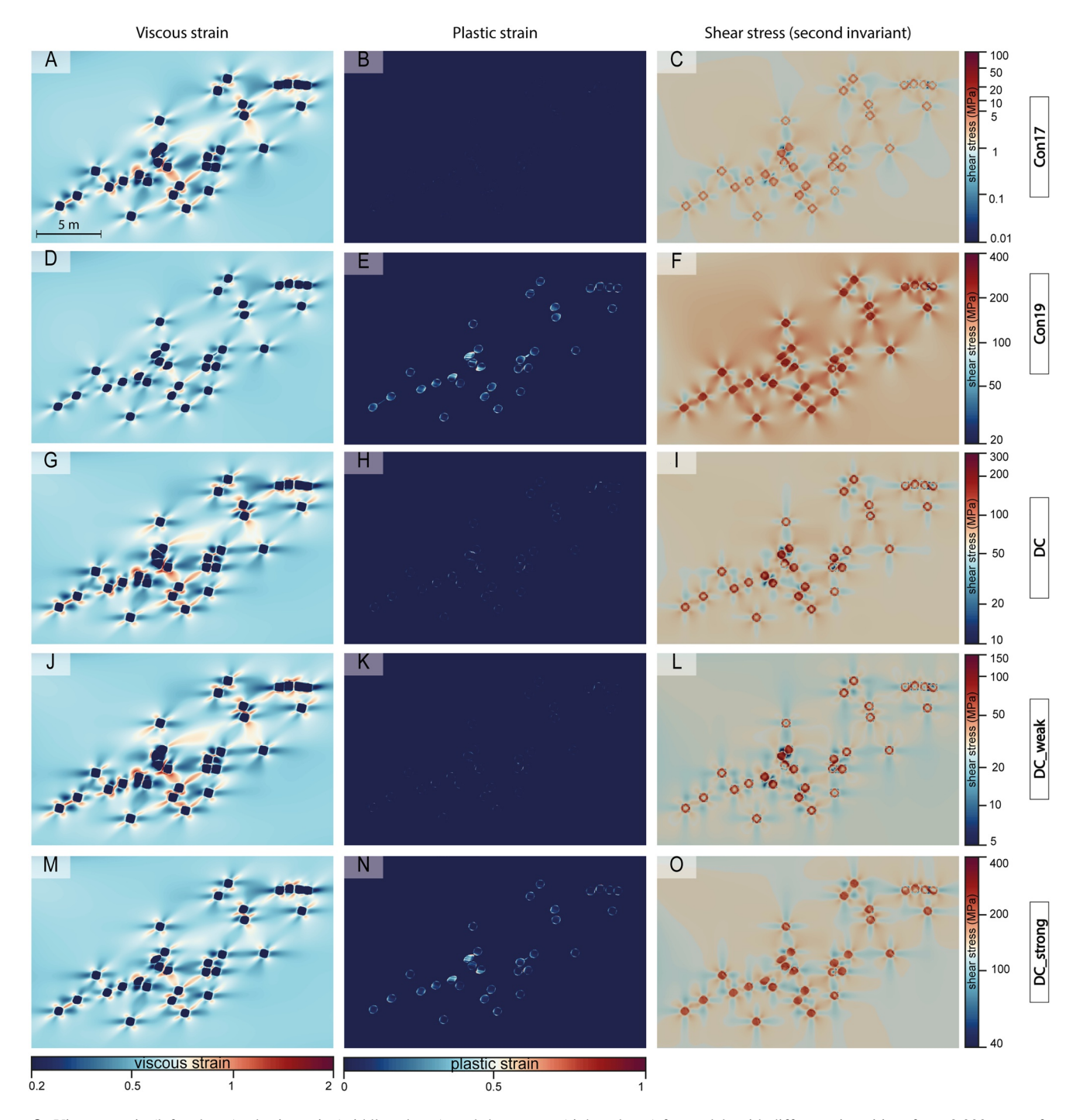


Figure 8. Viscous strain (left column), plastic strain (middle column), and shear stress (right column) for models with different viscosities after  $\sim$ 3,000 years of deformation: (a–c) for constant viscosity matrix of  $10^{19}$  Pa.s, (d–e) for constant viscosity matrix of  $10^{19}$  Pa.s, (g–i) for standard dislocation creep rheology for the matrix, (j–l) for weakened dislocation creep rheology for the matrix, and (m–o) for strengthened dislocation creep rheology for the matrix. The scale bar in panel (a) is the same for all models. *Note*. The different color-scale in all models for the second invariant of shear stress.

clasts have a shear stress of 2–6 MPa; this value can go locally as high as 50 MPa. Finally, the aspect ratio of the clasts does not change from the initial 1:1 (circle).

When the matrix viscosity is constant and large ( $10^{19}$  Pa.s), viscous shear strain of the matrix is less pronounced: again ~0.5 away from clasts, but only with a high of 0.84 and a low of 0.2 (Figure 8d). However, the viscous resistance of the matrix is high enough to transfer sufficient stress to the clasts, leading to pronounced deformation

IOANNIDI ET AL. 11 of 19



(Figure 8e). Strain does not localize only in the rims (with values between 0.2 and 0.6), but it penetrates some clasts (with plastic strain up to  $\sim$ 0.5). This results in elongation of clasts, which can reach aspect ratios up to 2:1. Shear stresses in the matrix range from 100 MPa away from clasts to 20 and 185 MPa in stress "shadows" and "peaks," respectively. Another difference from the previous model is the stress distribution in the clasts: here, stresses are more homogeneous and do not exhibit a large decrease toward the clast center. They range from 180 to 275 MPa (with an exceptionally high stress chain of >320 MPa, Figure 8f).

#### 4.3. Power-Law Matrix Viscosity

In the model with the standard dislocation creep parameters from Carter et al. (1981), for the given strain rate of  $\sim 10^{-11} \ s^{-1}$ , the resulting average matrix viscosity is  $\sim 5 \times 10^{18}$  Pa.s, while it can range between  $\sim 1 \times 10^{18}$  and  $\sim 1 \times 10^{20}$  Pa.s. Viscous strain localizes at the boundaries of clasts, mainly perpendicular to the  $\sigma_1$  stress orientation (Figure 8g). A bulk viscous strain of  $\sim 0.5$  is reached again, which locally can be as high as 1.8, in thin areas abutting clasts. In stress "shadows," viscous strain is  $\sim 0.2$ –0.3, while in stress "peaks" it is  $\sim 0.75$ . The clasts are plastically deformed but this deformation is much less pervasive when compared to the strong constant viscosity model (Figure 8h). The rims of clasts in clusters appear deformed, locally reaching a value of plastic strain of 1.0. Shear stress distribution is similar to that observed for the  $10^{17}$  Pa.s matrix, but it exhibits higher values (Figure 8i): homogeneous away from the clasts, and fluctuating around the clasts, with stress "peaks" and stress "shadows." The stresses supported by the viscous matrix are on the order of 55–60 MPa away from clasts, while they range from 20 to 80 MPa close to the clasts, depending on whether they are in a stress shadow or peak. Inside the clasts, stresses vary depending on their position relevant to other clasts (isolated vs. clustered clasts, clasts in the shadow or peak of other clasts). Similarly to the two-clast models, we notice "stress shadows" perpendicular to the  $\sigma_1$  axis (Figure 8i). The stresses in the clasts range between  $\sim 100$  and  $\sim 300$  MPa at their rims and decrease toward their centers ( $\sim 50$ –75 MPa). The shapes of the clasts remain the same, namely the aspect ratio is 1:1.

Models with the weakened dislocation creep law have a resulting viscosity of  $\sim 1 \times 10^{18}$  Pa.s, that can go up to  $\sim 4 \times 10^{18}$  Pa.s. This leads to a generally similar behavior of this model to that with the standard dislocation creep law, and hence to that with constant weak viscosity (compare also Figures 8a–8j). The viscous strain pattern is comparable to the aforementioned models, with similar values, although, as expected, strain in the matrix is slightly higher for the weakened viscosity model. The bulk strain is again  $\sim 0.5$ , while in shadows it is as low as 0.2 and as high as  $\sim 0.75$  in peaks (Figure 8j). In areas "sandwiched" between clasts, viscous strain may rise to 1.2. Clast deformation is also similar: plastic strain around some rims (on average 0.3, locally up to 0.8), but less extensive (Figure 8k). Shear stresses in this model are  $\sim 25$  MPa in the matrix away from clasts, while they fluctuate between  $\sim 10$  and  $\sim 35$  MPa in stress "shadows" and "peaks," respectively (Figure 8l). In clasts, the maximum stresses are  $\sim 130$  MPa and the minimum  $\sim 10$  MPa. Here, the aspect ratio of the clasts also remains 1:1.

The resulting viscosity for the matrix with the strengthened dislocation creep law is  $\sim 1 \times 10^{19}$  Pa.s away from clasts, and it varies between  $\sim 7 \times 10^{18}$  and  $\sim 2 \times 10^{19}$  Pa.s around them. The general behavior of this model resembles that of the constant high viscosity model, Con19 (compare e.g., Figures 8a–8c and 8m–8o). Viscous strain is  $\sim 2$  times smaller than in the previous two power-law viscosity models (Figure 8m). We observe again viscous strain of  $\sim 0.5$  away from the clasts, with a fluctuation between 0.15 and 1. Similarly to model Con19, some clasts exhibit strain only in their rims, while others deform also internally (Figure 8n). Plastic strain varies from < 0.1 to 0.85 in the rims; at clast centers, it is zero for internally undeformed clasts and can rise to 0.64 for the most deformed ones. Stresses are more homogeneous, the matrix exhibits values of  $\sim 125$  MPa away from clasts and with a range between 64 and 165 MPa (in stress shadows and peaks, respectively; Figure 8o). Similarly to model Con19, stresses in the clasts are more homogeneous, between  $\sim 200$  and 300 MPa. The high stress chain appears here, too, with values  $\sim 330$  MPa. Finally, the aspect ratio of the clasts ranges from 1:1 to 2:1.

#### 5. Discussion

#### 5.1. Model Conditions, Simplifications, and Limitations

The objective of this contribution is anchored in observations from the Papoose Flat pluton, where brittle feld-spar clasts show fractures at clast concentrations as low as 2% by area. The numerical models are designed to investigate the conditions, within the bounds of the natural prototype, that can lead to fracturing of brittle clasts embedded in a viscous matrix.

IOANNIDI ET AL. 12 of 19



#### **5.1.1.** Scaling

The measured "maps" from the field are  $30 \times 30$  cm in area, while our models are  $30 \times 30$  m in area. The motivation behind this change in scale is to facilitate relating our numerical observations to block dimensions that can potentially host transient slip events.

Previous work (Fagereng, 2011; Grigull et al., 2012; Ioannidi et al., 2021; Le Pourhiet et al., 2013) showed that the dimensions of blocks/structures do not affect the results of a model, as long as block distribution, strain rate and deformation mechanisms are the same at the different scales. Here, we created a numerical map representing the average block distribution of the field observations (7%). The range of strain rates suggested for the field varies between  $\sim 10^{-8}$  and  $\sim 10^{-12}$  s<sup>-1</sup>. Based on our initial conditions, the dimensions of our models and the shear velocities, the resulting strain rate ( $\sim 10^{-11}$  s<sup>-1</sup>) falls within this range (see also Discussion on strain rate, Section 5.1.2). The deformation mechanisms active on the micro-scale are dislocation creep in the matrix and frictional failure of the larger clasts. In our m-scale models, these two micro-deformation mechanisms remain the same. Therefore, maintaining the same block distribution, strain rate and deformation mechanisms, we can upscale the dimensions of our models from cm-to m-scales.

It should be noted that upscaling does not refer to the flow law used. When we change the scale from cm-scale field observations to m-scale models, we change only the size of the blocks and the imposed shear velocity resulting in the same strain rate on both scales (in this case  $\sim 10^{-11}~\rm s^{-1}$ ). The micromechanical properties and therefore constituent mineral phases are not scaled to actual dimensions. This means that by upscaling the granitic flow law of the matrix the individual components of the granite are not scaled. The size of the brittle clasts however increases with the scaling, leading to 1.5 m large feldspar clasts. While feldspar clasts of this size do not exist in nature, their mechanical behavior is equal to their cm-scale counterparts observed in the Papoose Flat pluton. Moreover, the clasts are modeled as a brittle phase inside a viscous matrix, without explicitly imposing a feld-spathic rheology. Therefore, these large feldspar clasts may reflect any kind of large brittle block in a viscous matrix, such as in a subduction mélange setting.

Finally, our models are sensitive to the choice of the dislocation creep law, as shown by the weaker and stronger rheologies (see also Figure A1, Text S1 and Figure S1 in Supporting Information S1). Our viscosity estimates are subject to uncertainties in the extrapolation of the experimental dislocation creep data. However, as long as the deformation mechanisms are similar, this extrapolation is well-grounded (Dimanov & Dresen, 2005).

#### 5.1.2. Strain Rate

As estimating the strain rate from field observations at the Papoose Flat pluton is not possible, we base our modeling strain rate choice of  $\sim 10^{-11}~\rm s^{-1}$  on findings by Chen and Nabelek (2017). Based on numerical models, the authors suggest that an incremental growth model for the formation of the Papoose Flat pluton is more realistic compared to a continuous intrusion model. For different types of growth models, they have calculated strain rates between  $2.5 \times 10^{-8}$  and  $5 \times 10^{-12}~\rm s^{-1}$ . It should be noted that the type of deformation in our models is sensitive to the strain rate. Consequently, choosing a strain rate close to the larger values of the suggested strain rate leads to extensive frictional failure in the model domain, especially for models with higher viscosities. However, deformation in the field shows no frictional deformation in the matrix, highlighting the necessity to choose a strain rate at the lower end of the proposed range by Chen and Nabelek (2017).

#### 5.1.3. Simple Shear Boundary Conditions and Total Strain

Field observations of the shear type at the Papoose Flat pluton are inconclusive. While shear fractures can be observed in the feldspar clasts away from the center of the pluton, the shear offset is small (Figure 2c). Some clasts display bookshelf structures, but they are not ubiquitous. Together with the formation of the viscous shear flow pattern and quartz ribbons and the absence of sigma clasts, they indicate some shear deformation with a modest amount of shear strain. Unfortunately, it is not possible to quantify the exact strain field and strain magnitude from field observations. We simplify the shear deformation in the numerical models to a simple shear boundary condition with a total bulk shear strain of 0.5.

#### 5.1.4. Impact of Viscosity Averaging Scheme

Viscosities are evaluated on material points, which need to be averaged before being projected onto the elements, and thus, the viscosity averaging scheme has an effect on the final solution. Usually, the arithmetic averaging

IOANNIDI ET AL. 13 of 19



gives the upper bound (making the elements on which viscosity is projected stiffer), while harmonic averaging gives the lower bound (making the element weaker). Geometric average represents the central tendency of the viscosities and lies between the arithmetic and harmonic averages. All three schemes may introduce numerical effects to the models. We cannot exclude that plastic strains at clasts rims in the three models with the lowest matrix viscosities are due to boundary effects. We, therefore, choose not to include these observations in our interpretation. However, less than 6% of all plastic markers have plastic strain values larger than 0.1. Therefore, we do not expected a significant effect on our modeling results. It should be noted that we do not see this behavior for the high viscosity models.

#### 5.2. Impact of Clast Spacing and Shape

To understand the effect of multiple clasts on the strain and stress distribution in the matrix and the clasts themselves we initially simplify the system to only two clasts. The strain and stress field perturbation around a single clast is well known and our models produce the anticipated patterns (e.g., Dabrowski et al., 2012; Jessell et al., 2009; Marques et al., 2014). As expected, if two clasts are located relatively close to each other their stress peaks and shadows interfere and govern their deformation pattern. This effect decreases with an increase in distance between clasts. Clasts that align parallel to the main stress direction ( $\sigma_1$ ) show stronger interaction compared to clasts that are not aligned with  $\sigma_1$ .

A difference between the field observations and the numerical models is the clast shape: the plagioclase clasts at the Papoose Flat pluton show predominantly rhombic shapes and a mean aspect ratio of 1.66. In our models, we simplify this geometry to circles, since both circles and rhombs have a similar behavior during shearing (Treagus, 2002).

#### 5.3. Impact of Clast Concentration

At the Papoose Flat pluton, we observe a weak correlation between clast concentration and the degree of failure within the clasts based on the number of fractured clasts, the area of fractured clasts, and the total fracture lengths. This correlation is however subject to some limitations. By using the number of fractured clasts, we assign clasts of varying sizes, with varying degrees of failure, and different fracture types the same value, leading to a non-representative weighing of clasts. When using the area of fractured clasts, we narrow some of the uncertainty of representation; however, there is still a source of inaccuracy due to the two-dimensional nature of the observations. The clasts as observed may not be characteristic of the three-dimensional system. Similarly, using the total fracture length within our two-dimensional observations is not fully representative of the brittle failure in three-dimensions. Contrary to expectations, brittle failure is observed at all clast concentrations, ranging from 2% to 12% by area; therefore, a critical concentration at which brittle failure begins to occur is not present.

This is confirmed by our numerical investigation for the high viscosity models, where all clasts show extensive brittle deformation, which is more pronounced in areas where clasts interact. Concurrently, clusters of clasts that are optimally oriented with respect to the  $\sigma_1$  axis show more extensive deformation. This would mean higher stresses and strains within these clasts, compared to isolated clasts. Neither in the field observations nor in the numerical models is the clast concentration high enough for forces to be transmitted via force chains (Cates et al., 1998; Peters et al., 2005).

#### 5.4. Matrix Rheology

While clast spacing and distribution have some impact on whether clasts break, this effect seems to be less relevant compared to the impact of the matrix viscosity. To break the clasts in the absence of clast-to-clast interaction, the viscous matrix needs to be able to support sufficiently high differential stresses.

While using a constant viscosity matrix is a clear simplification from the observations at the Papoose Flat pluton, it is also the simplest case in terms of rheology. Semi-frictional numerical experiments with constant viscosity matrix suggest that high viscosity contrasts between the matrix and the clasts can effectively lower the bulk shear stress required for clast failure (Beall et al., 2019a). In addition, analog experiments on elastic clasts embedded in a linear viscous matrix have shown that the matrix was able to sustain differential stresses over extended periods of time (Ladd & Reber, 2020).

IOANNIDI ET AL. 14 of 19



Our results for the low viscosity matrix (Con17) show some plastic strain at the rims of the clasts, which is possibly due to numerical artifacts introduced during viscosity averaging. It is clear, though, that shear stresses in the clasts are not high enough to deform/fracture them (Figures 8a–8c). In the model with high constant matrix viscosity (Con19), the matrix supports higher stresses, which in turn are transferred more effectively from the matrix to the clasts, causing the latter to deform plasticly.

The choice of dislocation creep to model the matrix is based on the dominant micro-deformation mechanism as presented by de Saint-Blanquat et al. (2001). We change the pre-exponential factor, A, to produce a weakened and a strengthened viscosity of the same material to better isolate the impact of the bulk viscosity on the stress transfer between matrix and clasts. This is not a new practice as numerical models of subduction zones have used similar configurations to simulate a weak subduction channel (e.g., Babeyko & Sobolev, 2008). Our results show that a stronger matrix can transfer stresses to the clasts and cause them to deform (model DC\_strong). Interestingly, a change in the A term only is enough to produce such a pronounced change in the bulk rheology of the system (e.g., from  $10^{18}$  to  $10^{20}$  Pa.s) and therefore has a strong effect on the deformability of the clasts. Both models with high matrix viscosity (constant and nonlinear) have the ability to transfer high enough stresses to the clasts to deform them plastically. However, in both cases a bulk matrix viscosity of  $\sim 10^{19}$  Pa.s is necessary.

#### 5.5. Implications for Slow Slip Models

The breaking of embedded strong patches in a viscous matrix (mélange formation) has been suggested to be one of the generation mechanisms for slow slip and tremor (SST) events (e.g., Fagereng & Sibson, 2010; Kirkpatrick et al., 2021; Kotowski & Behr, 2019; Phillips et al., 2020). Creeping sections of strike-slip and mega-thrust faults exhibit high micro-seismicity, which has been attributed to the failing of frictional patches (Beroza & Ide, 2011). Depending on the ratio between the brittle and the viscous phase, deformation dynamics can be fast for high brittle phase concentration; with an increase of the viscous phase, however, the slip speed will increasingly be dampened to the point where deformation will be creep like (Birren & Reber, 2019; Fagereng & Sibson, 2010; Reber et al., 2015). Slow slip events and tremor phenomena occur at a spatial scale that is orders of magnitude larger than the field examples and models presented here. When simplifying both systems to only two phases, however, small-scale observations might be transferable to SST phenomena. Our field observations and numerical investigations show that a brittle phase embedded in a viscous matrix can fail even at very low concentrations and modest bulk shear strains. The requirements to achieve brittle failure in isolated clasts is mainly dependent on a matrix rheology that can support high enough differential stresses, and to a lesser degree on the proximity to other clasts and the orientation with respect to the stress axes.

#### 6. Conclusions

The transition from frictional to viscous deformation in the Earth's crust is not sharp, but rather a finite zone where these two deformation types coexist. The resulting semi-frictional materials can be observed at scales ranging from millimeters to kilometers, where deformation on large scales might play an important role in understanding the transition from earthquakes to slow slip/creep. To study deformation of heterogeneous, semi-frictional materials, we use field observations from the Papoose Flat pluton, a Cretaceous granodiorite emplaced in the White-Inyo Range, in eastern California. The granitic matrix of the pluton constitutes the viscous phase, while the feldspar clasts form the brittle phase, the concentration of which varies between 2% and 12%. Field observations suggest increasing brittle failure of clasts with increasing clast concentration in the absence of a lower threshold for clast concentrations.

The complementary numerical models show that a clast that has a neighboring clast at a distance up to three times its diameter is affected significantly by the stress field of its neighbor. Concurrently, a one-order-of-magnitude increase in the nonlinear viscosity of the matrix results in almost two times higher strains in the matrix, extensive plastic deformation of the clasts, and three times higher shear stresses.

Our field observations and numerical investigations suggest that a brittle phase embedded in a viscous matrix can deform frictionally at very low concentrations and moderate bulk strains. The requirements to achieve frictional failure in isolated clasts are (a) a matrix rheology that can support high enough differential stresses over a period of time, and (b) a clast in its vicinity; however, it is not necessary that the clasts are in direct contact or even very close to each other. The orientation of clast clusters with respect to the direction of  $\sigma_1$ , as well as the strain rate

IOANNIDI ET AL. 15 of 19



may also enhance or prohibit their deformation. As long as the matrix material can support high stresses and transfer them to brittle clasts, similar processes are expected to occur in subduction mélanges responsible for a wide variety of seismic styles.

#### Appendix A

#### A1. Numerical Implementation

We use pTatin2D (May et al., 2014, 2015), an implementation of the Finite Element Method, which employs an Arbitrary Lagrangian Eulerian discretization, together with the material point method. We solve the Stokes equation (conservation of momentum), without gravity, due to the small size of our models:

$$\frac{\partial \sigma}{\partial x} = 0 \tag{A1}$$

and the full stress tensor,  $\sigma$ , is substituted by:

$$\sigma = \sigma^d - IP \tag{A2}$$

where  $\sigma^d$  is the deviatoric stress tensor, I the identity matrix, and P the dynamic pressure. The deviatoric stress tensor is computed for an effective viscosity,  $\eta_{\text{eff}}$ ,

$$\sigma^d = 2\eta_{\text{eff}}\dot{\varepsilon} \tag{A3}$$

with  $\dot{\varepsilon}$  being the strain rate tensor. We are interested in the steady-state long-term deformation of models, so elasticity is neglected, and the code approximates conservation of mass by enforcing incompressibility of flow, v:

$$\nabla \cdot v = 0 \tag{A4}$$

Material properties are assigned to material points in the computational domain which are advected with the velocity field of the solution from Stokes (Equation A1). The deviatoric stress is computed for the effective viscosity predicted by the dislocation creep law,  $\eta_{\text{eff}}^v$ , and for the effective viscosity predicted by the pressure-dependent Drucker-Prager yield criterion,  $\eta_{\text{eff}}^v$ . The rate-dependent effective viscosity,  $\eta_{\text{eff}}^v$ , is evaluated on material points by:

$$\eta_{\text{eff}}^{v} = \frac{1}{2} \left( \dot{\varepsilon}_{II}^{\frac{1}{2} - 1} A^{\frac{-1}{n}} \exp\left(\frac{Q}{RT}\right) \right) \tag{A5}$$

where  $\dot{\epsilon}_{II}$  is the second invariant of the strain rate tensor, R the gas constant, T the absolute temperature, and A, n, and Q the typical dislocation creep parameters obtained by deformation experiments, termed the pre-exponential constant, the stress sensitivity, and activation energy, respectively. The Drucker-Prager related viscosity is calculated by:

$$\eta_{\text{eff}}^p = \frac{\tau_y}{\dot{\epsilon}_{II}} \tag{A6}$$

where  $\tau_y$  is the yield strength of the material, calculated from the dynamic pressure, the internal friction angle,  $\varphi$ , and the cohesive strength, C:

$$\tau_y = P\sin\varphi - C\cos\varphi \tag{A7}$$

The effective viscosity,  $\eta_{\rm eff}$ , is therefore determined by

$$\eta_{\text{eff}} = \min \left[ \eta_{\text{eff}}^{v}, \eta_{\text{eff}}^{p} \right] \tag{A8}$$

and corresponds to the weakest mechanism. After being evaluated on material points, viscosity is projected to the Gauss points, using P0 projection and geometric averaging.

IOANNIDI ET AL. 16 of 19



#### A2. Strength Envelopes for Nonlinear Matrix Models

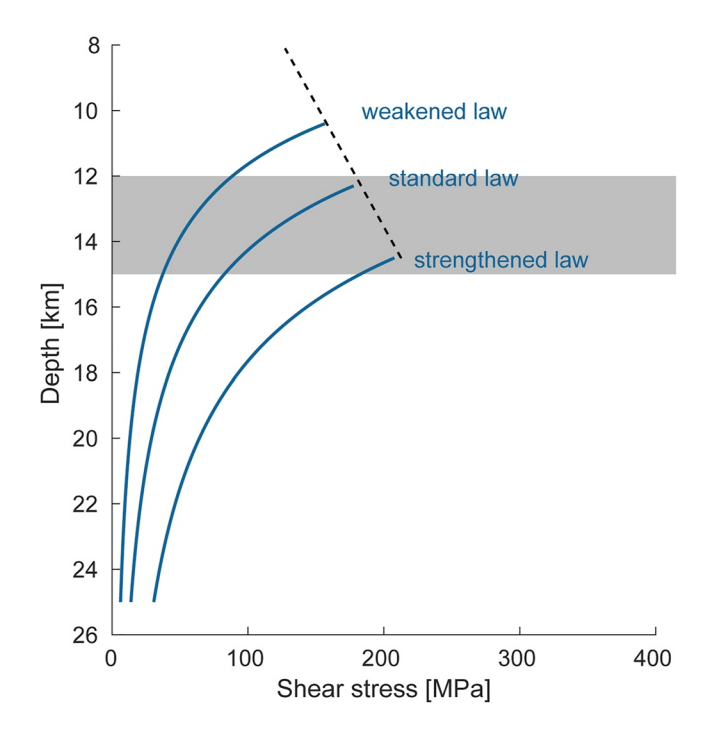


**Figure A1.** Strength envelope of flow laws used in our nonlinear viscous models. Dashed line represents frictional strength of the matrix (the same in all models). Blue curves from top to bottom correspond to models DC\_weak, DC, and DC\_strong and are calculated for a reference strain rate of  $1 \times 10^{-11}$  s<sup>-1</sup> and a geotherm of 30°C/km. Gray box represents the estimated depth of pluton emplacement, according to de Saint-Blanquat et al. (2001).

#### **Data Availability Statement**

The data used for this publication can be accessed via the Iowa State University data repository (https://doi.org/10.25380/iastate.16934038).

#### Acknowledgments

The authors were supported through NSF CAREER award #1843676. Thank you to Chris Ladd, Emily Ross, Collin Metz, and Sven Morgan for assistance in the field. P. I. Ioannidi acknowledges Gabriele Morra and Iskander Muldashev for fruitful numerical discussions. The authors thank Whitney Behr for the editorial handling and Susan Ellis and Noah Phillips for thoughtful comments and suggestions that improved this manuscript significantly.

#### References

Babeyko, A. Y., & Sobolev, S. V. (2008). High-resolution numerical modeling of stress distribution in visco-elasto-plastic subducting slabs. Lithos, 103(1-2), 205-216. https://doi.org/10.1016/j.lithos.2007.09.015

Beall, A., Fagereng, Å., & Ellis, S. (2019a). Strength of strained two-phase mixtures: Application to rapid creep and stress amplification in subduction zone mélange. *Geophysical Research Letters*, 46(1), 169–178. https://doi.org/10.1029/2018GL081252

Beall, A., Fagereng, Å., & Ellis, S. (2019b). Fracture and weakening of Jammed subduction shear zones, leading to the generation of slow slip events. *Geochemistry, Geophysics, Geosystems*, 20(11), 4869–4884. https://doi.org/10.1029/2019GC008481

Behr, W. M., & Bürgmann, R. (2021). What's down there? The structures, materials and environment of deep-seated slow slip and tremor. Philosophical Transactions of the Royal Society A: Mathematical, Physical & Engineering Sciences, 379(2193), 20200218. https://doi.org/10.1098/rsta.2020.0218

Behr, W. M., Kotowski, A. J., & Ashley, K. T. (2018). Dehydration-induced rheological heterogeneity and the deep tremor source in warm subduction zones. *Geology*, 46(5), 475–478. https://doi.org/10.1130/G40105.1

Beroza, G. C., & Ide, S. (2011). Slow earthquakes and nonvolcanic tremor. *Annual Review of Earth and Planetary Sciences*, 39(1), 271–296. https://doi.org/10.1146/annurev-earth-040809-152531

Birren, T., & Reber, J. E. (2019). The impact of rheology on the transition from stick-slip to creep in a semibrittle analog. *Journal of Geophysical Research: Solid Earth*, 124(3), 3144–3154. https://doi.org/10.1029/2018JB016914

Bürgmann, R. (2018). The geophysics, geology and mechanics of slow fault slip. Earth and Planetary Science Letters, 495, 112–134. https://doi.org/10.1016/j.epsl.2018.04.062

Carter, N. L., Anderson, D. A., Hansen, F. D., & Kranz, R. L. (1981). Creep and creep rupture of granitic rocks. In N. Carter, M. Friedman, J. Logan, & D. Stearns (Eds.), Mechanical Behavior of Crustal Rocks, https://doi.org/10.1029/GM024p0061

Cates, M. E., Wittmer, J. P., Bouchaud, J. P., & Claudin, P. (1998). Jamming, force chains, and fragile matter. *Physical Review Letters*, 81(9), 1841–1844. https://doi.org/10.1103/PhysRevLett.81.1841

Chen, Y., & Nabelek, P. I. (2017). The influences of incremental pluton growth on magma crystallinity and aureole rheology: Numerical modeling of growth of the Papoose Flat pluton, California. *Contributions to Mineralogy and Petrology*, 172, 89. https://doi.org/10.1007/s00410-017-1405-6 Dabrowski, M., Schmid, D. W., & Podladchikov, Y. Y. (2012). A two-phase composite in simple shear: Effective mechanical anisotropy development and localization potential. *Journal of Geophysical Research*, 117. https://doi.org/10.1029/2012JB009183

IOANNIDI ET AL. 17 of 19



- de Saint-Blanquat, M., Law, R. D., Bouchez, J. L., & Morgan, S. S. (2001). Internal structure and emplacement of the Papoose Flat pluton: An integrated structural, petrographic, and magnetic susceptibility study. *Bulletin of the Geological Society of America*, 113(8), 976–995. https://doi.org/10.1130/0016-7606(2001)113<0976:ISAEOT>2.0.CO;2
- Dimanov, A., & Dresen, G. (2005). Rheology of synthetic anorthite-diopside aggregates: Implications for ductile shear zones. *Journal of Geophysical Research*, 110, B07203. https://doi.org/10.1029/2004JB003431
- Einstein, A. (1905). Über die von der molekularkinetischen Theorie der Wärme geforderte Bewegung von in ruhenden Flüssigkeiten suspendierten Teilchen. *Annalen der Physik*, 322(8), 549–560. https://doi.org/10.1002/andp.19053220806
- Fagereng, Å. (2011). Fractal vein distributions within a fault-fracture mesh in an exhumed accretionary mélange, Chrystalls Beach Complex, New Zealand. Journal of Structural Geology, 33(5), 918–927. https://doi.org/10.1016/j.jsg.2011.02.009
- Fagereng, Å., & Sibson, R. H. (2010). Mélange rheology and seismic style. Geology, 38(8), 751–754. https://doi.org/10.1130/G30868.1
- Fusseis, F., Handy, M. R., & Schrank, C. (2006). Networking of shear zones at the brittle-to-viscous transition (Cap de Creus, NE Spain). *Journal of Structural Geology*, 28(7), 1228–1243. https://doi.org/10.1016/j.jsg.2006.03.022
- Gapais, D., Bale, P., Choukroune, P., Cobbold, P. R., Mahjoub, Y., & Marquer, D. (1987). Bulk kinematics from shear zone patterns: Some field examples. *Journal of Structural Geology*, 9(5–6), 635–646. https://doi.org/10.1016/0191-8141(87)90148-9
- Grigull, S., Krohe, A., Moos, C., Wassmann, S., & Stöckhert, B. (2012). "Order from chaos": A field-based estimate on bulk rheology of tectonic mélanges formed in subduction zones. *Tectonophysics*, 568–569, 86–101. https://doi.org/10.1016/j.tecto.2011.11.004
- Handy, M. R. (1990). The solid-state flow of polymineralic rocks. *Journal of Geophysical Research*, 95(B6), 8647–8661. https://doi.org/10.1029/ib095ib06p08647
- Hayman, N. W., & Lavier, L. L. (2014). The geologic record of deep episodic tremor and slip. *Geology*, 42(3), 195–198. https://doi.org/10.1130/G34990.1
- Higashi, N., & Sumita, I. (2009). Experiments on granular rheology: Effects of particle size and fluid viscosity. *Journal of Geophysical Research*, 114(4). https://doi.org/10.1029/2008JB005999
- Hirth, G., & Tullis, J. (1992). Dislocation creep regimes in quartz aggregates. *Journal of Structural Geology*, 14(2), 145–159. https://doi.org/10.1016/0191-8141(92)90053-Y
- Holyoke, C. W., & Tullis, J. (2006). Mechanisms of weak phase interconnection and the effects of phase strength contrast on fabric development. Journal of Structural Geology, 28(4), 621–640. https://doi.org/10.1016/j.jsg.2006.01.008
- Ioannidi, P. I., Le Pourhiet, L., Agard, P., Angiboust, S., & Oncken, O. (2021). Effective rheology of a two-phase subduction shear zone: Insights from numerical simple shear experiments and implications for subduction zone interfaces. *Earth and Planetary Science Letters*, 566, 116913. https://doi.org/10.1016/j.epsl.2021.116913
- Jammes, S., Lavier, L. L., & Reber, J. E. (2015). Localization and delocalization of deformation in a bimineralic material. *Journal of Geophysical Research: Solid Earth*, 120(5), 3649–3663. https://doi.org/10.1002/2015JB011890
- Jessell, M. W., Bons, P. D., Griera, A., Evans, L. A., & Wilson, C. J. L. (2009). A tale of two viscosities. Journal of Structural Geology, 31(7), 719–736. https://doi.org/10.1016/j.jsg.2009.04.010
- Johnson, S. E., Vernon, R. H., & Upton, P. (2004). Foliation development and progressive strain-rate partitioning in the crystallizing carapace of a tonalite pluton: Microstructural evidence and numerical modeling. *Journal of Structural Geology*, 26(10), 1845–1865. https://doi.org/10.1016/j.jsg.2004.02.006
- Jordan, P. G. (1987). The deformational behaviour of bimineralic limestone-halite aggregates. Tectonophysics, 135(1-3), 185–197. https://doi.org/10.1016/0040-1951(87)90160-0
- Jourdon, A., Le Pourhiet, L., Petit, C., & Rolland, Y. (2018). The deep structure and reactivation of the Kyrgyz Tien Shan: Modelling the past to better constrain the present. *Tectonophysics*, 746, 530–548. https://doi.org/10.1016/j.tecto.2017.07.019
- Kirby, S. H., & Kronenberg, A. K. (1987). Rheology of the lithosphere: Selected topics. Reviews of Geophysics, 25, 1680–1681.
- Kirkpatrick, J. D., Fagereng, Å., & Shelly, D. R. (2021). Geological constraints on the mechanisms of slow earthquakes. *Nature Reviews Earth & Environment*, 2, 285–301. https://doi.org/10.1038/s43017-021-00148-w
- Kotowski, A. J., & Behr, W. M. (2019). Length scales and types of heterogeneities along the deep subduction interface: Insights from exhumed rocks on Syros Island, Greece. Geosphere, 15(4), 1038–1065. https://doi.org/10.1130/GES02037.1
- Ladd, C. R., & Reber, J. E. (2020). The effect of a liquid phase on force distribution during deformation in a granular system. *Journal of Geophysical Research: Solid Earth*, 125(8). https://doi.org/10.1029/2020JB019771
- Lavier, L. L., Bennett, R. A., & Duddu, R. (2013). Creep events at the brittle ductile transition. *Geochemistry, Geophysics, Geosystems*, 14(9), 3334–3351. https://doi.org/10.1002/ggge.20178
- Le Pourhiet, L., Huet, B., Labrousse, L., Yao, K., Agard, P., & Jolivet, L. (2013). Strain localisation in mechanically layered rocks beneath detachment zones: Insights from numerical modelling. *Solid Earth*, 4, 135–152. https://doi.org/10.5194/se-4-135-2013
- Li, L., Addad, A., Weidner, D., Long, H., & Chen, J. (2007). High pressure deformation in two-phase aggregates. Tectonophysics, 439(1-4), 107-117. https://doi.org/10.1016/j.tecto.2007.04.004
- Marques, F. O., Mandal, N., Taborda, R., Antunes, J. V., & Bose, S. (2014). The behaviour of deformable and non-deformable inclusions in viscous flow. Earth-Science Reviews, 134, 16–69. https://doi.org/10.1016/j.earscirev.2014.03.007
- May, D. A., Brown, J., & Le Pourhiet, L. (2014). pTatin3D: High-performance methods for long-term lithospheric dynamics. In Proceedings of the International Conference for High Performance Computing, Networking, Storage and Analysis, SC '14, (pp. 274–284). https://doi. org/10.1109/SC.2014.28
- May, D. A., Brown, J., & Le Pourhiet, L. (2015). A scalable, matrix-free multigrid preconditioner for finite element discretizations of heterogeneous Stokes flow. Computer Methods in Applied Mechanics and Engineering, 290, 496–523. https://doi.org/10.1016/j.cma.2015.03.014
- Mitra, S. (1976). A quantitative study of deformation mechanisms and finite strain in quartzites. Contributions to Mineralogy and Petrology, 59, 203–226. https://doi.org/10.1007/BF00371309
- Morgan, S. S., Law, R. D., & de Saint Blanquat, M. (2000). Papoose Flat, Eureka Valley–Joshua Flat–Beer Creek, and Sage Hen Flat plutons: Examples of rising, sinking, and cookie-cutter plutons in the central White–Inyo Range, eastern California. In D. R. Lageson, S. G. Peters, & M. M. Lahren (Eds.), Great Basin and Sierra Nevada. https://doi.org/10.1130/0-8137-0002-7.189
- Morgan, S. S., Law, R. D., & Nyman, M. W. (1998). Laccolith-like emplacement model for the Papoose Flat pluton based on porphyroblast-matrix analysis. *Bulletin of the Geological Society of America*, 110(1), 96–110. https://doi.org/10.1130/0016-7606(1998)110<0096:LLEMFT>2.3.CO;2
  Passchier, C. W., & Trouw, R. A. J. (2005). *Microtectonics*. Springer-Verlag. https://doi.org/10.1007/3-540-29359-0
- Paterson, S. R., Brudos, T., Fowler, K., Carlson, C., Bishop, K., & Vernon, R. H. (1991). Papoose Flat pluton: Forceful expansion or postemplacement deformation? *Geology*, 19(4), 324–327. https://doi.org/10.1130/0091-7613(1991)019<0324:PFPFEO>2.3.CO;2
- Peters, J. F., Muthuswamy, M., Wibowo, J., & Tordesillas, A. (2005). Characterization of force chains in granular material. *Physical Review E Statistical, Nonlinear and Soft Matter Physics*, 72, 041307. https://doi.org/10.1103/PhysRevE.72.041307

IOANNIDI ET AL. 18 of 19



- Phillips, N. J., Motohashi, G., Ujiie, K., & Rowe, C. D. (2020). Evidence of localized failure along altered basaltic blocks in tectonic mélange at the updip limit of the seismogenic zone: Implications for the shallow slow earthquake source. *Geochemistry, Geophysics, Geosystems*, 21(7). https://doi.org/10.1029/2019GC008839
- Reber, J. E., Hayman, N. W., & Lavier, L. L. (2014). Stick-slip and creep behavior in lubricated granular material: Insights into the brittle-ductile transition. *Geophysical Research Letters*, 41(10), 3471–3477. https://doi.org/10.1002/2014GL059832
- Reber, J. E., Lavier, L. L., & Hayman, N. W. (2015). Experimental demonstration of a semi-brittle origin for crustal strain transients. *Nature Geoscience*, 8, 712–715. https://doi.org/10.1038/ngeo2496
- Roscoe, R. (1952). The viscosity of suspensions of rigid spheres. British Journal of Applied Physics, 3, 267–269. https://doi.org/10.1088/0508-3443/3/8/306
- Ross, D. C. (1966). Stratigraphy of some Paleozoic formations in the Independence Quadrangle Inyo County, California. Geological Survey Professional Paper, 1–17. https://doi.org/10.3133/pp396
- Scholz, C. H. (1998). Earthquakes and friction laws. Nature, 391, 37-42. https://doi.org/10.1038/34097
- Sylvester, A. G., Ortel, G., Nelson, C. A., & Christie, J. M. (1978). Papoose Flat pluton: A granitic blister in the Inyo Mountains, California. Bulletin of the Geological Society of America, 89(8), 1205–1219. https://doi.org/10.1130/0016-7606(1978)89<1205:PFPAGB>2.0.CO;2
- Treagus, S. H. (2002). Modelling the bulk viscosity of two-phase mixtures in terms of clast shape. *Journal of Structural Geology*, 24(1), 57–76. https://doi.org/10.1016/S0191-8141(01)00049-9
- Wakefield, J. (1977). Mylonitization in the Lethakane shear zone, eastern Botswana. Journal of the Geological Society, 133(3), 263–275. https://doi.org/10.1144/gsjgs.133.3.0263
- Webber, S., Ellis, S., & Fagereng, Å. (2018). "Virtual shear box" experiments of stress and slip cycling within a subduction interface mélange. Earth and Planetary Science Letters, 488, 27–35. https://doi.org/10.1016/j.epsl.2018.01.035

#### **References From the Supporting Information**

Hansen, F. D., & Carter, N. L. (1982). Creep of selected crustal rocks at 1000 MPa. Eos: Transactions – American Geophysical Union, 63, 437.
Ranalli, G. (1997). Rheology of the lithosphere in space and time. Geological Society, London, Special Publications, 121, 19–37. https://doi.org/10.1144/GSL.SP.1997.121.01.02

IOANNIDI ET AL. 19 of 19